AIAA JOURNAL
Vol. 46, No. 4, April 2008

Effect of Stiffness Uncertainties on the Flutter of a Cantilever Wing

S. C. Castravete* and R. A. Ibrahim†
Wayne State University, Detroit, Michigan 48202

DOI: 10.2514/1.31692

This paper deals with the investigation of the influence of spanwise distribution of bending and torsion stiffness uncertainties on the flutter behavior of an aeroelastic wing using a stochastic finite element approach. The analysis adopted a numerical algorithm to simulate unsteady, nonlinear, incompressible flow (based on the unsteady vortex lattice method) interacting with linear aeroelastic structure in the absence of uncertainties. The airflow and wing structure are treated as elements of a single dynamic system. Parameter uncertainties are represented by a truncated Karhunen–Love expansion. Both perturbation technique and Monte Carlo simulation are used to establish the boundary of stiffness uncertainty level, at which the wing exhibits flutter in the form of limit-cycle oscillations and above which the wing experiences dynamic instability. The analysis also includes the limitation of perturbation solution for a relatively large level of stiffness uncertainty.

Nomenclature

A	=	wing cross-sectional area
$C(y, y_1)$	=	covariance kernel
c	=	factor accounting for the noncircular geometry of the wing cross section
E	=	Young's modulus
$\mathbf{F}_A(t)$	=	total aerodynamic force vector
$\mathbf{F}_{A,P}$	=	aerodynamic load vector at point P
$\mathbf{F}_s$	=	assembled elemental force vector
F_u, F_v, F_w	=	external global forces acting along x, y, and z directions, respectively
f_n	=	set of deterministic functions in the Karhunen-Loeve expansion
G	=	modulus of rigidity
I_0	=	wing mass moment of inertia (about inertia axis) per unit length
I_x	=	area moment of inertia of the wing cross section about x axis
I_z	=	area moment of inertia of the wing cross section about z axis
J	=	polar moment of inertia of the wing cross section about z axis
$\mathbf{K}^e$	=	elemental stiffness matrix of wing structure
$\mathbf{K}_0$, $\mathbf{K}_0^e$	=	mean values of assembled and elemental stiffness matrices of the wing, respectively
$\mathbf{K}_{b,n}$, $\mathbf{K}_{t,n}$	=	bending and torsion random stiffness matrices, respectively
$\mathbf{K}_{b,n}^e$, $\mathbf{K}_{t,n}^e$	=	elemental bending and torsion random stiffness matrices, respectively
L	=	wing length
L_C	=	chordwise length of an element of the bound lattice
l_{cor}	=	spatial correlation length of wing uncertain parameters
$\mathbf{M}$, $\mathbf{M}^e$	=	assembled and elemental mass matrix of the wing, respectively
M_α	=	external moment acting on the wing about its inertia axis
m	=	mass of the wing per unit length
ND	=	number of degrees of freedom of the finite element model
NM	=	maximum number of mode shapes used in the analyses
$\mathbf{n}$	=	unit normal vector at a control point
p	=	aerodynamic pressure at a point P on the lattice
p_∞	=	airflow pressure
$\mathbf{q}$	=	generalized coordinates vector
q_{ben}, q_{tor}	=	first bending and first torsion generalized coordinates
$\mathbf{R}_0$, $\mathbf{r}_0$	=	position vectors of point P^0 in the inertial and body frames, respectively
T_C	=	characteristic time
$\mathbf{U}$, $\mathbf{U}^e$	=	assembled and elemental vectors of the displacements of the points in the structural grid, respectively
$\tilde{u}$, $\tilde{v}$, $\tilde{w}$	=	global displacements along x, y, and z directions
u_i, v_i, w_i	=	nodal displacements in x, y, and z directions
$\mathbf{V}_F$	=	absolute velocity of the flow
$\mathbf{V}_\infty$	=	freestream velocity
${}^N\bar{\mathbf{v}}^B(\tau)$	=	absolute nondimensional velocity of the origin of the body frame B
$Y_{j=1,2,\ldots,6}$	=	shape functions
$\tilde{\alpha}$	=	global torsion angle
β_i, α_i, γ_i	=	nodal rotations about$x$, y, and z axes, respectively
δ_3	=	distance between elastic and inertia axes of the wing structure
δ_{nm}	=	Kronecker delta
θ	=	parameter that belongs to the space of random events
$\mathbf{\Lambda}$	=	truncated diagonal matrices of eigenvalues, respectively
λ_n	=	constants in the Karhunen–Loeve expansion
ξ_n	=	set of random variables with zero mean
ρ_∞	=	density of the fluid
$\sigma_{\text{ben}}^2 = E[s_{\text{ben}}^2]$, $\sigma_{\text{tor}}^2 = E[s_{\text{tor}}^2]$	=	variances of bending and torsion response, respectively
$\sigma_{EI_x}^2$, σ_{GJ}^2	=	variances of bending and torsion stiffness random fields, respectively

Received 30 April 2007; revision received 7 December 2007; accepted for publication 11 December 2007.

*Senior Project Engineer; currently CAELYNX, 3850 Research Park Drive, Ann Arbor, MI 48108; stefan@caelynx.com.

†Professor, Department of Mechanical Engineering; ibrahim@eng.wayne.edu.

$\tau = t/T_C$ = nondimensional time
χ, $\bar{\chi}$, σ_χ^2 = random field, its mean value, and its variance, respectively
Ψ = truncated eigenvector matrix, respectively
${}^N\bar{\omega}^B$ = nondimensional angular velocity of the B frame
ω_n = eigenvalues of the characteristic equation in the Karhunen–Loeve expansion

I. Introduction

THE presence of parameter uncertainties in aeroelastic structures adds a new dimension to an already complicated problem. Parameter uncertainties owe their origin to a number of sources, which include 1) randomness in material properties due to variations in material composition, 2) randomness in structural dimensions due to manufacturing variations and thermal effects, 3) randomness in boundary conditions due to preload and relaxation variations in mechanical joints, and 4) randomness of external excitations.

Generally, uncertainty is described as either parametric or nonparametric. Parametric uncertainty is due to variability in the value of input parameters, whereas nonparametric uncertainty includes all other sources, such as modeling errors, coarse finite element mesh fidelity, or unmodeled nonlinear effects.

Parameter uncertainties may cause sensitivity and variability of the response and eigenvalues of structural stochasticity [1–3]. The early developments relied on Monte Carlo simulation and, later on, first- and second-order perturbation methods to compute second-order moments of structure response. Furthermore, the general sources of uncertainty affecting the design and testing of aeroelastic structures were discussed. In particular, Pettit [3] addressed a number of applications of uncertainty quantification to various aeroelastic problems such as flutter flight testing, prediction of limit-cycle oscillations (LCO), and design optimization with aeroelastic constraints. Different computational methodologies have been employed [4,5] to quantify the uncertain response of aeroelastic structures with parametric variability. These methodologies include finite element and perturbation methods.

One of the major problems of incorporating the random field into finite element analyses is to deal with abstract spaces which have limited physical support [6,7]. The difficulty involves the treatment of random variables defined on these abstract spaces. Usually, the problem is solved through Monte Carlo simulation or stochastic finite element methods. Because of the large number of samples, which require high computational time, the Monte Carlo simulation is used mainly to verify other approaches. The perturbation [8–11] and Neumann expansion [10,12] methods proved acceptable results for small random variation in the material properties. It was found that these methods are comparable in accuracy, but the most efficient solution procedure is the perturbation finite element method, which requires a single simulation. However, perturbation method requires the system uncertainty to be small enough to guarantee convergence and accurate results.

The perturbation stochastic finite element method (SFEM) has been adopted by several researchers using the Karhunen–Loeve (K-L) expansion to discretize the random fields due to structure mechanical properties [13–15]. Jensen [16] considered an extension of the deterministic finite element method to the space of random function. A Neumann dynamic SFEM of vibration for structures with stochastic parameters under random excitation was treated by Lei and Qiu [17]. The equation of motion was transformed into a quasi-static equilibrium equation for the solution of displacement in time domain. The Neumann expansion method was applied to the equation for deriving the statistical solution of the dynamic response within the framework of Monte Carlo simulation. The K-L expansion has proven to be a powerful tool in modeling parameter uncertainties in the structural dynamics community. However, it has not been used in the randomness and variability of parameters in aeroelastic structures. The present work is an attempt to employ the K-L expansion to discretize the spanwise distribution of bending and torsion stiffness uncertainties of an aircraft wing.

Structural and material uncertainties have a direct impact on the flutter characteristics of aeroelastic structures and they have begun to attract some attention in the literature. They were considered in studying the flutter of panels and shells [18–22]. Liaw and Yang [18,19] quantified the effect of parameter uncertainties on the reduction of the structural reliability and stability boundaries of initially compressed laminated plates and shells. For buckling analysis, the uncertainties were included in the modulus of elasticity, thickness, and fiber orientation of individual lamina, as well as geometric imperfections. For flutter analysis, further uncertainties such as mass density, air density, and in-plane load were also considered. Kuttenkeuler and Ringertz [20] performed an optimization study of the onset of flutter, with respect to material and structural uncertainties using finite element analysis and the doublet-lattice method. Lindsley et al. [21,22] considered uncertainties in the modulus of elasticity and boundary conditions for a nonlinear panel in supersonic flow. The probabilistic response distributions were obtained using Monte Carlo simulation. It was reported that uncertainties have the greatest nonlinear influence on LCO amplitude near the deterministic point of LCO. Poirion [23,24] employed a first-order perturbation method to solve for the probability of flutter given uncertainty in the structural mass and stiffness operators.

Recently, the influence of parameter uncertainties on the response of a typical airfoil section was considered by a few researchers [25–28]. The sensitivity of uncertainty of aeroelastic phenomena was evaluated using Monte Carlo simulation. The effect of parametric uncertainty on the response of a nonlinear aeroelastic system was studied by Attar and Dowell [28] using a response surface method to map the random input parameters to the root-mean square wing tip response.

Civil engineers have been involved in studying the influence of uncertainties of structural properties, in particular, damping, on the reliability analysis of flutter of a bridge girder and a flat plate was determined in a few studies [29–31]. The prediction of the flutter wind speed was found to be associated with a number of uncertainties such that the critical wind speed can be treated as a stochastic variable. The probability of the bridge failure due to flutter was defined as the probability of the flutter speed exceeding the extreme wind speed at the bridge site for a given period of time. The probabilistic dynamic response of a wind-excited structure has been studied in terms of uncertain parameters such as wind velocity, and lift and drag coefficients by Kareem [32]. The influence of uncertainty in these parameters was found to propagate in accordance with the functional relationships that relate them to the structural response. Note that in aerospace structures, one is interested in estimating the onset flutter due to parameter uncertainty; civil engineers, on the other hand, focus on probabilistic reliability analysis to determine a probability of the bridge or a structure failure due to flutter for a given return period rather than stating a single critical wind speed.

A ground vibration test was used by Potter and Lind [33] to obtain uncertainty models, such as natural frequencies and their associated variations, which can update analytical models for the purpose of predicting robust flutter speeds. Different norm approaches were used to formulate uncertainty models that cover the entire range of observed variations. Lind and Brenner [34] introduced a tool referred to as the "flutterometer" for predicting the onset of flutter during a flight test. The flutterometer computes the onset of flutter for an analytical model with respect to an uncertainty description. Brenner [35] considered a technique that identifies model parameters and their associated variances from flight data. Later, Prazenica et al. [36] introduced a technique for estimating uncertainty descriptions based on a wavelet approach, but relies on Volterra kernels.

The present work deals with the influence of stiffness uncertainties on the flutter behavior of an aeroelastic wing. A numerical algorithm originally developed by Preidikman and Mook [37] to simulate unsteady, nonlinear, incompressible flow interacting with a linear aeroelastic wing in the absence of uncertainties is adopted. To implement this algorithm in the presence of uncertainties, we introduce a random field that represents bending or torsion stiffness

parameters, or both, as a truncated Karhunen–Love expansion [6]. The airflow and wing structure are treated as elements of a single dynamic system. Both perturbation technique and Monte Carlo simulation are used to establish the boundary of stiffness uncertainty level, at which the wing exhibits LCO and above which the wing experiences dynamic instability. The analysis also includes the limitation of perturbation solution for a relatively large level of stiffness uncertainty. The analytical modeling of aerodynamic loading based on the unsteady vortex lattice method, structural forces interacting with the aerodynamic loading, and stiffness uncertainties based on the K-L expansion are briefly described in Secs. II, III, and IV, respectively. Section V establishes the entire system modeling by combining the three models (aerodynamic, structure, and uncertainty) in the wing governing equations of motion in the finite element discretized form. Sections VI and VII present the perturbation analysis solution and Monte Carlo simulation results, respectively, together with a comparison of the corresponding results.

II. Aerodynamic Modeling

Aerodynamic modeling requires the estimation of aerodynamic forces and, at the same time, accounts for a wing elastic deformation. This is achieved by using the unsteady vortex lattice method. The lifting surface is approximated by a set of lattices of short segments of constant circulation each. Each segment occupies a portion of the wing surface and is enclosed by a loop of vortex segments. Figure 1a shows the discretization of the lifting surface, in which N frame is the ground fixed coordinate system and B frame is the coordinate system on the wing body and is moving with the wing. The leading segment of the vortex loop is located at a distance equivalent to a quarter of the panel length. The velocities are calculated at a finite number of points called control or collocation points located at the lattice center. Figure 1b represents the position of an arbitrary control point P on the lattice as a result of the wing structure displacement.

The point P^0 represents the point P before the wing is deformed. In the N frame, the positions of P^0 and P are given by the vectors $\mathbf{R}_0$ and $\mathbf{R}$, respectively. The corresponding vectors in the B frame are $\mathbf{r}_0$ and $\mathbf{r}$. The displacement of the aerodynamic point P due to deformation of the wing is $\Delta\mathbf{r}_{A_P}$. The vectors $\mathbf{R}$ and $\mathbf{r}$ can be represented as functions of the wing displacement $\Delta\mathbf{r}_{A_P}$, i.e., $\mathbf{R} = \mathbf{R}_0 + \Delta\mathbf{r}_{A_P}$ and $\mathbf{r} = \mathbf{r}_0 + \Delta\mathbf{r}_{A_P}$. The pressure $p(t)$ at point P was estimated using Bernoulli's equation for unsteady flow from which the nondimensional aerodynamic load at point P is [38]

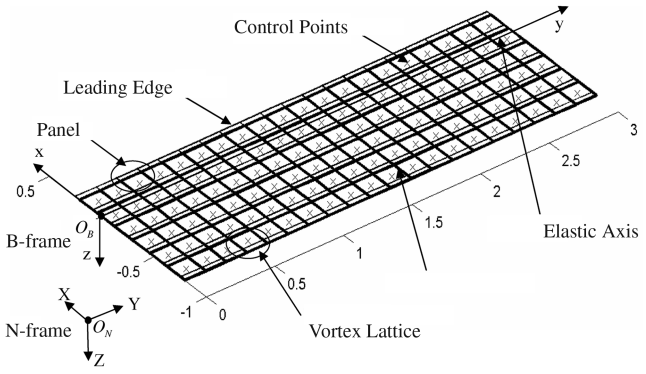

a)

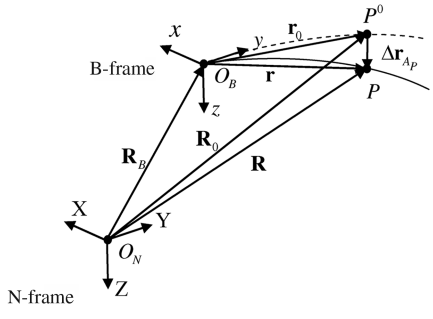

b)

Fig. 1 Discretization and coordinate frames of a lifting surface: a) lifting surface discretization, b) position of an arbitrary point P on the lifting surface caused by the wing structure deformation.

$$\bar{\mathbf{F}}_{A,P}(\tau) = 2\left\{\Delta\bar{\mathbf{V}}_P \cdot [\bar{\mathbf{V}}_{mP} - {}^N\bar{\mathbf{v}}^B - {}^B\bar{\dot{\mathbf{r}}}^P - \bar{\boldsymbol{\omega}}^B \cdot {}^B\bar{\mathbf{r}}^P] + \frac{D}{D\tau}[\bar{G}_P]\right\}\bar{A}_P\mathbf{n} \tag{1}$$

where $\mathbf{n}$ is the unit normal vector at the control point, $\bar{A}_P = A_P/L_C^2$ is the nondimensional area of the element P, A_P is the area of the element, L_C represents the chordwise length of one element on the bound lattice, $\tau = t/T_C$, $\bar{\mathbf{R}} = \mathbf{R}/L_C = \bar{\mathbf{R}}_0 + \Delta\bar{\mathbf{r}}_{A_P}$, $\bar{\mathbf{R}}_0 = \mathbf{R}_0/L_C$, $\Delta\bar{\mathbf{r}}_{A_P} = \Delta\mathbf{r}_{A_P}/L_C$, $T_C = L_C/V_\infty$ is a characteristic time, $\bar{\mathbf{V}}_F = \mathbf{V}_F/V_\infty$, $\mathbf{V}_F$ is the absolute velocity of the airflow, $\mathbf{V}_\infty$ is the freestream velocity. $\Delta\bar{\mathbf{V}}_P = \Delta\mathbf{V}_P/\mathbf{V}_\infty$ is the nondimensional tangential velocity difference across the vortex lattice and $\bar{\mathbf{V}}_{mP}$ is the "mean" velocity, which does not recognize the presence of the local vorticity. $\bar{\mathbf{V}}_{m,P}$ can be considered as the flow velocity at the midpoint of the vortex sheet thickness. $\bar{G}_P$ is the circulation loop in nondimensional form of the vortex lattice element which encloses the control point P, ${}^N\bar{\mathbf{v}}^B(\tau)$ is the absolute velocity of O_B, ${}^B\bar{\mathbf{r}}^P$ and ${}^B\bar{\dot{\mathbf{r}}}^P$ are the position and velocity of P relative to the B frame, respectively, and ${}^N\bar{\boldsymbol{\omega}}^B(\tau)$ is the angular velocity of the B frame. The expression for the aerodynamic load at point P in dimensional form is

$$\mathbf{F}_{A,P}(t) = \left[\left(\rho_\infty V_\infty^2/2\right)L_C^2\right]\bar{\mathbf{F}}_{A,P}(\tau) \tag{2}$$

where ρ is the density of the fluid. This aerodynamic force is acting at the center of each lattice and interacts with the elastic and inertia forces of the wing structure, and their modeling is given in the next section.

III. Structural Modeling

Figure 2a shows a cantilever wing with a straight elastic axis at distance δ_3 from the inertia axis. The wing is structurally modeled as an Euler–Bernoulli beam. The coordinate system coincides with the B frame coordinate system from the aerodynamic modeling. The wing is divided into elements as shown in Fig. 2b, whereas a single element with two nodes is shown in Fig. 2c.

The displacements of each element, $\tilde{u}(y,t)$, $\tilde{\mathrm{v}}(y,t)$, and $\tilde{w}(y,t)$, are expressed in terms of the nodal displacements u_i, v_i, w_i in x, y, and z directions, respectively, and nodal rotations $\beta_i, \alpha_i, \gamma_i$ about x, y, and z axes, respectively. The relationships between the element and nodal displacements are

$$\tilde{u}(y,t) = \mathbf{Y}_u^T(y)\mathbf{u}_e(t), \qquad \tilde{\mathrm{v}}(y,t) = \mathbf{Y}_v^T(y)\mathbf{v}_e(t)$$

$$\tilde{w}(y,t) = \mathbf{Y}_w^T(y)\mathbf{w}_e(t)$$

$$\tilde{\alpha}(y,t) = \mathbf{Y}_\alpha^T(y)\boldsymbol{\alpha}_e(t) \quad \text{where } \mathbf{Y}_u^T(y) = \mathbf{Y}_w^T(y) = \{Y_3 \;\; Y_5 \;\; Y_4 \;\; Y_6\}$$

$$\mathbf{Y}_v^T(y) = \mathbf{Y}_\alpha^T(y) = \{Y_1 \;\; Y_2\}$$

$$\mathbf{u}_e = \begin{Bmatrix} u_i \\ \gamma_i \\ u_{i+1} \\ \gamma_{i+1} \end{Bmatrix}, \qquad \mathbf{v}_e = \begin{Bmatrix} \mathrm{v}_i \\ \mathrm{v}_{i+1} \end{Bmatrix}$$

$$\mathbf{w}_e(t) = \begin{Bmatrix} w_i \\ \beta_i \\ w_{i+1} \\ \beta_{i+1} \end{Bmatrix}, \qquad \boldsymbol{\alpha}_e(t) = \begin{Bmatrix} \alpha_i \\ \alpha_{i+1} \end{Bmatrix} \tag{3}$$

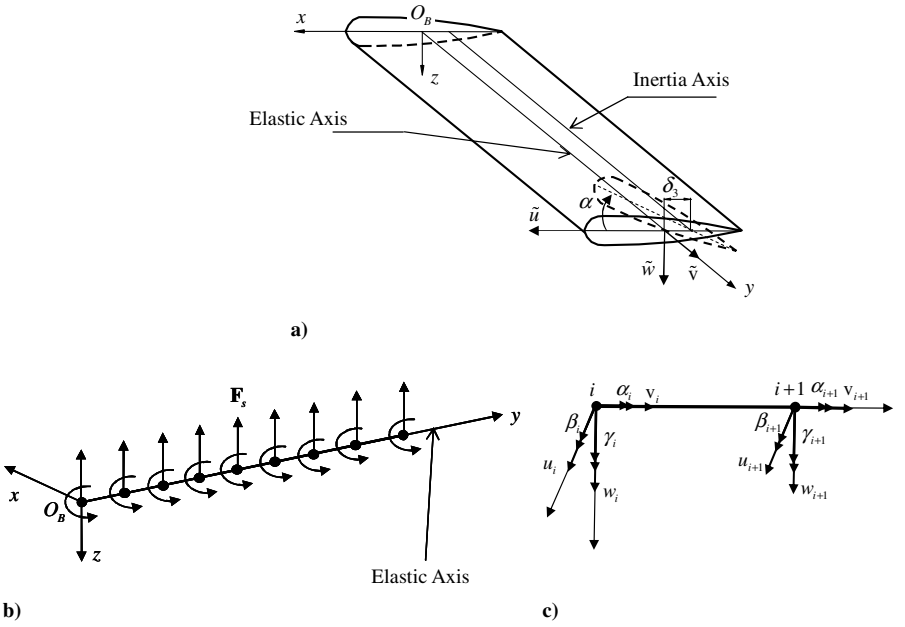

Fig. 2 Cantilever wing and its discretizations: a) schematic diagram of a cantilever wing model, b) finite elements discretization, c) finite element representation.

Y_j, $j = 1, 2, \ldots, 6$ the shape functions given by Chandrupatla and Belegundu [39]. Applying Lagrange's equation to each coordinate gives the following set of equations of motion:

$$m\left(\int_{y_i}^{y_{i+1}} \mathbf{Y}_u(y)\mathbf{Y}_u(y)^T\,\mathrm{d}y\right)\ddot{\mathbf{u}}_e(t) + \left(\int_{y_i}^{y_{i+1}} EI_z\mathbf{Y}_u(y)''[\mathbf{Y}_u(y)'']^T\,\mathrm{d}y\right)\mathbf{u}_e(t) = \int_{y_i}^{y_{i+1}} F_u\mathbf{Y}_u(y)\,\mathrm{d}y \tag{4a}$$

$$m\left(\int_{y_i}^{y_{i+1}} \mathbf{Y}_v(y)\mathbf{Y}_v(y)^T\,\mathrm{d}y\right)\ddot{\mathbf{v}}_e(t) + \left(\int_{y_i}^{y_{i+1}} AE\mathbf{Y}_v(y)'[\mathbf{Y}_v(y)']^T\,\mathrm{d}y\right)\mathbf{v}_e(t) = \int_{y_i}^{y_{i+1}} F_v\mathbf{Y}_v(y)\,\mathrm{d}y \tag{4b}$$

$$m\left(\int_{y_i}^{y_{i+1}} \mathbf{Y}_w(y)\mathbf{Y}_w(y)^T\,\mathrm{d}y\right)\ddot{\mathbf{w}}_e(t) + m\delta_3\left(\int_{y_i}^{y_{i+1}} \mathbf{Y}_w(y)\mathbf{Y}_\alpha(y)^T\,\mathrm{d}y\right)\ddot{\boldsymbol{\alpha}}_e(t) + \left(\int_{y_i}^{y_{i+1}} EI_x\mathbf{Y}_w(y)''[\mathbf{Y}_w(y)'']^T\,\mathrm{d}y\right)\mathbf{w}_e(t) = \int_{y_i}^{y_{i+1}} F_w\mathbf{Y}_w(y)\,\mathrm{d}y \tag{4c}$$

$$\left(\int_{y_i}^{y_{i+1}} I_\alpha\mathbf{Y}_\alpha(y)\mathbf{Y}_\alpha(y)^T\,\mathrm{d}y\right)\ddot{\boldsymbol{\alpha}}_e(t) + m\delta_3\left(\int_{y_i}^{y_{i+1}} \mathbf{Y}_\alpha(y)\mathbf{Y}_w(y)^T\,\mathrm{d}y\right)\ddot{\mathbf{w}}_e(t) + \left(\int_{y_i}^{y_{i+1}} cGJ\mathbf{Y}_\alpha(y)'[\mathbf{Y}_\alpha(y)']^T\,\mathrm{d}y\right)\boldsymbol{\alpha}_e(t) = \int_{y_i}^{y_{i+1}} M_\alpha\mathbf{Y}_\alpha(y)\,\mathrm{d}y \tag{4d}$$

where a prime denotes a derivative with respect to spatial variable y. The mass per unit length is m , I_0 is mass moment of inertia (about inertia axis) per unit length, and L is the wing length. A is the wing cross-sectional area, E is Young's modulus, I_x is the area moment of inertia of the wing cross section about x axis, I_z is the area moment of inertia of the wing cross section about z axis, J is the polar moment of inertia of the wing cross section about z axis, G is the modulus of rigidity, and c is a factor accounting for the noncircular geometry of the wing cross section. The value of c depends on the cross section geometry and is documented in the literature [40]. F_u, F_v, and F_w are the external forces acting along x, y, and z axes, respectively, and M_α is the external moment about the inertia axis. Equations (4) may be written in the matrix form

$$\mathbf{M}^e\ddot{\mathbf{U}}^e + \mathbf{K}^e\mathbf{U}^e = \mathbf{F}^e \tag{5}$$

where $\mathbf{U}^e = \{u_i\ v_i\ w_i\ \beta_i\ \alpha_i\ \gamma_i\ u_{i+1}\ v_{i+1}\ w_{i+1}\ \beta_{i+1}\ \alpha_{i+1}\ \gamma_{i+1}\}^T$.

Equation (5) constitutes the governing equations of motion for a single element without uncertainties. The inclusion of material uncertainties will be considered in the next section.

IV. Modeling of Material Uncertainties

Material uncertainty is considered for bending and torsion stiffness parameters. Let the bending and torsion stiffness parameters be represented in the form

$$EI_x(y) = \overline{EI}_x + \widetilde{EI}_x(y), \qquad GJ(y) = \overline{GJ} + \widetilde{GJ}(y) \tag{6a}$$

The mean values $\overline{EI}_x \gg 0$ and $\overline{GJ} \gg 0$ are assumed to be much larger than the root mean square of the random field variability represented by $\widetilde{EI}_x(y)$ and $\widetilde{GJ}(y)$. Both $\widetilde{EI}_x(y)$ and $\widetilde{GJ}(y)$ are assumed to be Gaussian distributed with zero mean and their standard deviations σ_{EI_x} and σ_{GJ} are much smaller than the corresponding mean value, i.e., $\sigma_{EI_x}/\overline{EI}_x \ll 1$ and $\sigma_{GJ}/\overline{GJ} \ll 1$. This implies that the stiffness parameters $EI_x(y)$ and $GJ(y)$ form positive-valued random fields. Let the stiffness parameters be represented by the random function $\chi(y, \theta)$, where θ is a parameter that belongs to the space of random events and $y \in [-L/2, L/2]$. The random field $\chi(y, \theta)$ can be expressed by the truncated K-L expansion [6]:

$$\chi(y, \theta) = \bar{\chi}(y) + \sum_{n=1}^{N} \xi_n(\theta)\sqrt{\lambda_n}f_n(y) \tag{6b}$$

where $\bar{\chi}(y)$ is the mean value of $\chi(y,\theta)$, λ_n are the eigenvalues of the random field as defined in Eqs. (7) and (9b), $f_n(y)$ is a set of eigenfunctions, and $\xi_n(\theta)$ is a set of random variables with zero mean, and $E[\xi_n(\theta)\xi_m(\theta)] = \delta_{nm}$, δ_{nm} is the Kronecker delta. Where λ_n are the eigenvalues of the covariance operators in Eqs. (7) and (8), and $f_n(y)$ are the corresponding eigenfunctions by the solution of the integral equation

$$\int_{-L/2}^{L/2} C(y,y_1) f_n(y_1)\,\mathrm{d}y_1 = \lambda_n f_n(y) \tag{7}$$

where $C(y,y_1)$ is the covariance kernel of the random field $\chi(y,\theta)$.

Expansion (6b) is mathematically well founded and is guaranteed to converge. The convergence and accuracy of the K-L expansion were proven by Huang et al. [41] by comparing the second-order statistics of the simulated random process with that of the target process. It was shown that the factors affecting convergence are mainly the ratio of the length of the process over the correlation parameter and the form of the covariance function. The K-L expansion has an advantage over the spectral analysis for highly correlated processes. For long stationary processes, the spectral method is generally more efficient, as the K-L expansion method requires substantial computational effort to solve the integral equation. In addition, it is optimum in the sense that it minimizes the mean square error resulting from truncating the series at a finite number of terms. The bending and torsion stiffness parameters will be modeled by one-dimensional Gaussian random field models with bounded mean squares. Ghanem and Spanos [6] and Loeve [42] showed that, for a Gaussian process, the K-L expansion converges. The covariance kernel of the random field $\chi(y,\theta)$ may be assumed in the form

$$C(y,y_1) = \sigma_\chi^2 e^{-|y-y_1|/l_{\mathrm{cor}}} \tag{8}$$

where σ_χ^2 is the variance of the random field χ, such that $\sigma_\chi \ll \bar{\chi}(y)$, implying that $\chi(y,\theta)$ will always be positive, l_{cor} is the correlation length such that $l_{\mathrm{cor}} \to L$. For the one-dimensional case, the eigenvalue problem Eq. (7) possesses the closed form analytical solution [6]

$$f_n(y) = \frac{\cos(\omega_n y)}{\sqrt{(L/2) + [\sin(2\omega_n L/2)/2\omega_n]}} \tag{9a}$$

$$\lambda_n = \frac{2\sigma_\chi^2/l_{\mathrm{cor}}}{\omega_n^2 + 1/l_{\mathrm{cor}}^2} \tag{9b}$$

where ω_n are the roots of the characteristic equation

$$\left[\frac{1}{l_{\mathrm{cor}}} - \omega\tan\left(\omega\frac{L}{2}\right)\right]\left[\omega + \frac{1}{l_{\mathrm{cor}}}\tan\left(\omega\frac{L}{2}\right)\right] = 0 \tag{10}$$

Introducing the expressions of Eq. (9) into Eq. (6) the random field takes the following form:

$$\chi(y,\theta) = \bar{\chi}(y) + \sum_{n=1}^{N} 2\xi_n(\theta)\sigma_\chi \sqrt{\frac{\omega_n/l_{\mathrm{cor}}}{(\omega_n^2 + 1/l_{\mathrm{cor}}^2)[L\omega_n + \sin(2\omega_n L/2)]}}\cos(\omega_n y) \tag{11}$$

For bending stiffness, the random field χ is denoted by $EI_x(y)$ with mean value $\overline{EI}_x$ and variance $\sigma_{EI_x}^2$; for torsion stiffness, the random field χ is denoted by $GJ(y)$ with mean value $\overline{GJ}$ and variance σ_{GJ}^2. For simplicity, it is assumed that both parameters are uncorrelated. The elemental stiffness expression $\mathbf{K}^e$ is

$$\mathbf{K}^e(\theta) = \mathbf{K}_0^e + \sum_{n=1}^{N} \mathbf{K}_{b,n}^e \xi_n(\theta) + \sum_{n=1}^{N} \mathbf{K}_{t,n}^e \xi_n(\theta) \tag{12}$$

where

$$\mathbf{K}_0^e = EI_z \int_{y_i}^{y_{i+1}} \mathbf{Y}_u''(\mathbf{Y}_u'')^T\,\mathrm{d}y + AE\int_{y_i}^{y_{i+1}} \mathbf{Y}_v'(\mathbf{Y}_v')^T\,\mathrm{d}y + \overline{EI}_x \int_{y_i}^{y_{i+1}} \mathbf{Y}_w''(\mathbf{Y}_w'')^T\,\mathrm{d}y + c\overline{GJ}\int_{y_i}^{y_{i+1}} \mathbf{Y}_\alpha'\mathbf{Y}_\alpha'^T\,\mathrm{d}y \tag{13a}$$

$$\mathbf{K}_{b,n}^e = \int_{y_i}^{y_{i+1}} 2\xi_n(\theta)\sigma_{EI_x} \times \sqrt{\frac{\omega_n/l_{\mathrm{cor}}}{(\omega_n^2 + 1/l_{\mathrm{cor}}^2)[L\omega_n + \sin(2\omega_n L/2)]}}\cos(\omega_n y)\mathbf{Y}_w''\mathbf{Y}_w''^T\,\mathrm{d}y \tag{13b}$$

$$\mathbf{K}_{t,n}^e = \int_{y_i}^{y_{i+1}} 2\xi_n(\theta)\sigma_{GJ} \times \sqrt{\frac{\omega_n/l_{\mathrm{cor}}}{(\omega_n^2 + 1/l_{\mathrm{cor}}^2)[L\omega_n + \sin(2\omega_n L/2)]}}\cos(\omega_n y)\mathbf{Y}_\alpha'\mathbf{Y}_\alpha'^T\,\mathrm{d}y \tag{13c}$$

Assembling the elemental matrices, we obtain

$$\mathbf{M}\ddot{\mathbf{U}}(\theta) + \left[\mathbf{K}_0 + \left(\sum_{n=1}^{N}\mathbf{K}_{b,n}\xi_n(\theta)\right) + \left(\sum_{n=1}^{N}\mathbf{K}_{t,n}\xi_n(\theta)\right)\right]\mathbf{U}(\theta) = \mathbf{F}_s(\mathbf{U}) \tag{14}$$

where $\mathbf{M}$ is a $(6n_S \cdot 6n_S)$ mass matrix which represents the assembled elemental mass matrix $\mathbf{M}^e$, n_S is the number of points in the structural grid, $\mathbf{K}_0$ is a $(6n_S \cdot 6n_S)$ matrix representing the assembled elemental mean value of the stiffness matrix $\mathbf{K}_0^e$. $\mathbf{K}_{b,n}$ and $\mathbf{K}_{t,n}$ are $(6n_S \cdot 6n_S)$ matrices representing the assembled elemental bending $\mathbf{K}_{b,n}^e$ and torsion $\mathbf{K}_{t,n}^e$ random stiffness matrices, respectively. $\mathbf{F}_s(\mathbf{U},t,\theta)$ is a $(6n_S \cdot 1)$ vector representing the assembled elemental force vector $\mathbf{F}_s^e$, and $\mathbf{U}(t,\theta)$ is a $(6n_S \cdot 1)$ vector of the displacements of the points in the structural grid and represents the assembled elemental displacement vector $\mathbf{U}^e$.

Note that the left-hand side of Eq. (14) constitutes a set of stochastic second-order differential equations with random variable coefficients with Gaussian distribution. In the absence of aerodynamic forces, these equations are always stable, because the stiffness matrices are real positive definite. This is guaranteed by the fact that the uncertain components of the stiffness parameters are very small compared with their mean values, as stated in the beginning of this section. In the next section, the aerodynamic nodes will be connected to the structural finite element mesh and the aerodynamic forces will be transferred to the structural grid.

V. System Modeling

Figure 3a shows the structural grid superimposed to the aerodynamic grid. The relationship between the displacements of the aerodynamic grid points and displacements of the structural grid points is

$$\Delta\underline{\Re}_A = \begin{Bmatrix} \Delta\mathbf{r}_1 \\ \Delta\mathbf{r}_2 \\ \vdots \\ \Delta\mathbf{r}_{n_A} \end{Bmatrix} = \mathbf{G}_{AS}\mathbf{U} \tag{15}$$

where $\Delta\underline{\Re}_A$ is a $(3n_A \cdot 1)$ vector representing the displacements of the control points in the aerodynamic grid, n_A is the number of control points in the aerodynamic grid, $\mathbf{G}_{AS}$ is a $3n_A \cdot 6n_S$ interpolation matrix that connects the displacements of the nodal points in the aerodynamic grid to the displacements of the nodal points in the structural grid [37].

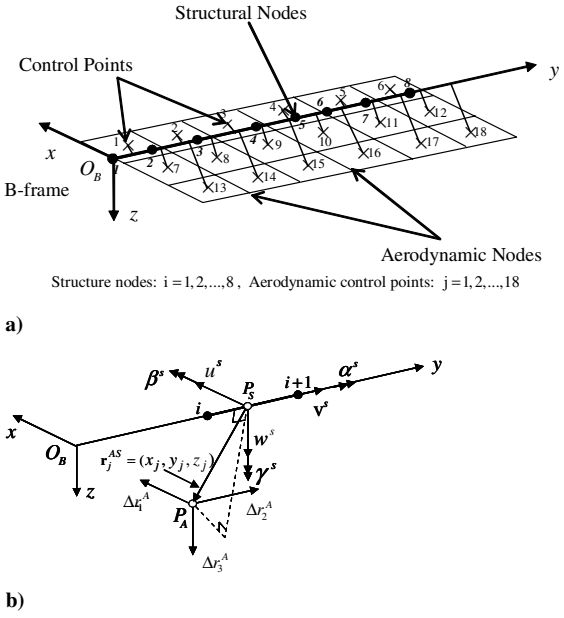

Fig. 3 Structural and aerodynamic discretizations: a) structural grid superimposed to the aerodynamic grid, b) connection of an aerodynamic grid point to an internal point of the structural grid point.

Figure 3b shows how an aerodynamic point is connected to an internal structural grid point, where an aerodynamic point P_A is connected to a point P_S on the elastic axis between two successive structural nodes. For the present study, the structural nodes are labeled by the index i, where $i = 1, 2, \ldots, 8(=n_s)$, whereas the aerodynamic points are labeled by the index j, where $j = 1, 2, \ldots, 18(=n_A)$. The points P_S and P_A are in the same plane, which is perpendicular to the elastic axis. The relative position between P_A and P_S is given by the vector $\mathbf{r}_j^{AS} = (x_j, y_j, z_j)$. The displacement of the point P_A is given by $\Delta\mathbf{r}_j^A = \{\Delta r_1^A, \Delta r_2^A, \Delta r_3^A\}^T$ and the displacement of the point P_S is given by $\mathbf{U}_i = \{u_i^s, v_i^s, w_i^s, \beta_i^s, \alpha_i^s, \gamma_i^s\}^T$. The relationship between the points P_A and P_S is given by [38]

$$\Delta\mathbf{r}_{j_A} = \tilde{\mathbf{G}}_{ji}\mathbf{U}_{i_S}, \qquad \tilde{\mathbf{G}}_{ji} = \begin{bmatrix} 1 & 0 & 0 & 0 & z_j & 0 \\ 0 & 1 & 0 & -z_j & 0 & x_j \\ 0 & 0 & 1 & 0 & -x_j & 0 \end{bmatrix} \tag{16}$$

The displacement vector $\mathbf{U}_{P_S}$ is obtained by finite element interpolation as a function of displacements on nodes i and $i+1$ as follows [37]:

$$\mathbf{U}_{P_S} = \begin{bmatrix} \mathbf{Y}_{11} & \mathbf{Y}_{12} & \mathbf{Y}_{13} & \mathbf{Y}_{14} \\ \mathbf{Y}_{21} & \mathbf{Y}_{22} & \mathbf{Y}_{23} & \mathbf{Y}_{24} \end{bmatrix}\mathbf{U}_{i,i+1} = \tilde{\mathbf{Y}}\mathbf{U}_{i,i+1} \tag{17}$$

Where $\mathbf{U}_{i,i+1} = \{u_i\ v_i\ w_i\ \beta_i\ \alpha_i\ \gamma_i\ u_{i+1}\ v_{i+1}\ w_{i+1}\ \beta_{i+1}\ \alpha_{i+1}\ \gamma_{i+1}\}^T$, and the detailed structures of $\mathbf{Y}_{ij}$ are given in the Appendix. Introducing Eq. (17) into Eq. (16) gives

$$\Delta\mathbf{r}_{j_A} = [\tilde{\mathbf{G}}_{ji}\tilde{\mathbf{Y}}]\begin{Bmatrix}\mathbf{U}_i \\ \mathbf{U}_{i+1}\end{Bmatrix} = [\mathbf{G}_{j,i}\ \ \mathbf{G}_{j,i+1}]\begin{Bmatrix}\mathbf{U}_i \\ \mathbf{U}_{i+1}\end{Bmatrix} \tag{18}$$

Next, the matrix $\mathbf{G}_{j,i}$ will be assembled into the global matrix $\mathbf{G}_{AS}$, which is introduced into Eq. (15). To obtain the relationship between the aerodynamic forces $\mathbf{F}_A$ and structural forces $\mathbf{F}_S$, the two force systems must have the same work for any virtual displacement, i.e.,

$$\delta(\Delta\underline{\mathfrak{R}}_A)^T\mathbf{F}_A = \delta\mathbf{U}_{\mathrm{St}}^T\{(\mathbf{G}_{AS})^T\mathbf{F}_A\} = \delta\mathbf{U}_{\mathrm{St}}^T\mathbf{F}_S \tag{19}$$

where $\delta(\Delta\underline{\mathfrak{R}}_A)$ and $\delta\mathbf{U}_{\mathrm{St}}^T$ are virtual displacements of control points of the aerodynamic grid and of structural nodes, respectively. $\mathbf{G}_{AS}$ is the global matrix which connects the control points of the aerodynamic grid to the structural grid points, $\mathbf{F}_A$ is the matrix of aerodynamic force, which is located at the aerodynamic control point, and $\mathbf{F}_S$ is the matrix of the structural load, which is located at the structural grid points. Equation (19) yields the relationship between structural forces and the aerodynamic forces,

$$\mathbf{F}_S = (\mathbf{G}_{AS})^T\mathbf{F}_A = \mathbf{G}_{SA}\mathbf{F}_A \tag{20}$$

where $(\mathbf{G}_{AS})^T = \mathbf{G}_{SA}$. Introducing Eq. (20) into Eq. (14), the equations of motion of the system is

$$\mathbf{M}\ddot{\mathbf{U}}(\theta) + \left[\mathbf{K}_0 + \left(\sum_{n=1}^{N}\mathbf{K}_{b,n}\xi_n(\theta)\right) + \left(\sum_{n=1}^{N}\mathbf{K}_{t,n}\xi_n(\theta)\right)\right]\mathbf{U}(\theta) = \mathbf{G}_{SA}\mathbf{F}_A(\theta) \tag{21}$$

Equation (21) constitutes the equations of motion of a wing involving stiffness uncertainties. A modal analysis of Eq. (21) is performed and gives

$$\mathbf{K}_0\tilde{\mathbf{\Psi}} = \mathbf{M}\tilde{\mathbf{\Psi}}\,\tilde{\mathbf{\Lambda}} \tag{22}$$

where $\tilde{\mathbf{\Psi}}$ is an $\mathbb{N}\cdot\mathbb{N}$ eigenvector matrix where $\mathbb{N}$ is the number of degrees of freedom of the finite element model, and $\tilde{\mathbf{\Lambda}}$ is an $\mathbb{N}\cdot\mathbb{N}$ diagonal matrix of eigenvalues. Equation (21) will be solved using perturbation analysis in the next section.

VI. Perturbation Analysis

To develop the perturbation analysis, it is convenient to introduce the following coordinate transformation, which approximates the deformation of the beam:

$$\mathbf{U}(t,\theta) \cong \sum_{k=1}^{\tilde{N}}\Psi_k q_k = \mathbf{\Psi}\mathbf{q} \tag{23a}$$

where $\mathbf{\Psi}$ is a truncated form of $\tilde{\mathbf{\Psi}}$. For the present application, the method requires the displacement vector be expanded into the truncated Taylor series:

$$\mathbf{U}(t,\theta) = \mathbf{\Psi}\left[\mathbf{q}_0(t) + \sum_{n=1}^{N}\left.\frac{\partial\mathbf{q}}{\partial\xi_n}\right|_{\xi=0}\xi_n(\theta) + \frac{1}{2}\sum_{n=1}^{N}\sum_{m=1}^{N}\left.\frac{\partial^2\mathbf{q}}{\partial\xi_n\partial\xi_m}\right|_{\xi=0}\xi_n(\theta)\xi_m(\theta) + \ldots\right] \tag{23b}$$

Note that $\mathbf{\Psi}$ is an $\mathbb{N}\cdot\tilde{N}$ matrix that includes first $\tilde{N}$ mode shape vector, $\mathbf{q}$ is an $\tilde{N}\cdot 1$ generalized coordinates vector, and $\mathbf{q}_0$ is the mean value of $\mathbf{q}$. Substituting Eq. (23b) into Eq. (21), premultiplying both sides by $\mathbf{M^{-1}\Psi^T}$, and collecting terms of the same power of ξ yields a set of perturbational equations of zero-order, first-order, second-order, and so on. For simplification sake, we restrict the analysis up to the first-order and the following perturbational equations are obtained:

Zero-order equation (coefficients of ξ_n^0):

$$\ddot{\mathbf{q}}_0 + [\mathbf{\Psi}^T\mathbf{K}_0\mathbf{\Psi}]\mathbf{q}_0 = [\mathbf{M^{-1}\Psi^T G}_{SA}]\mathbf{F}_{A,0} \tag{24a}$$

First-order equation (coefficients of ξ_n^1):

$$\ddot{\mathbf{q}}_{1,n} + [\mathbf{\Psi}^T\mathbf{K}_0\mathbf{\Psi}]\mathbf{q}_{1,n} = -[\mathbf{\Psi^T K}_{b,n}\mathbf{\Psi} + \mathbf{\Psi^T K}_{t,n}\mathbf{\Psi}]\mathbf{q}_0 + [\mathbf{M^{-1}\Psi^T G}_{SA}]\frac{\partial\mathbf{F}_A}{\partial\xi_n} \tag{24b}$$

where $n = 1\ldots N$, $\mathbf{q}_{1,n} = \partial\mathbf{q}/\partial\xi_n$, and $[\mathbf{\Psi}^T\mathbf{K}_0\mathbf{\Psi}]$ is an $\tilde{N}\cdot\tilde{N}$ diagonal matrix of first $\tilde{N}$ eigenvectors. The aerodynamic loading $\mathbf{F}_A$, as defined by Eq. (1), depends on the wing displacement $\Delta\mathbf{r}_{Ap}$ which is time dependent. Note that $\partial\mathbf{F}_A/\partial\xi_n$ is obtained by taking the derivative of Eq. (1) with respect to ξ_n after substituting for $\Delta\mathbf{r}_{Ap}$, which is expressed in Eqs. (16) and (23b) which is a function of ξ_n.

Equations (24) are numerically integrated once using an adapted Hamming's fourth-order predictor-corrector method. The numerical solutions are performed using the following values of the wing [43]: $\overline{EI}_x = 10^6$ Nm^2, $EI_z = 50 \cdot 10^6$ Nm^2, $\overline{GJ} = 1.5 \cdot 10^6$ Nm^2, $EA = 20 \cdot 10^6$ N, $m = 10$ kg/m, $I_0 = 15$ kgm^2/m, $\delta_3 = 0.15$ m, wing length $L = 3$ m, wing chord $C = 1$ m, angle of attack $\alpha_a = 5$ deg, $L_C = 0.16667$ m, and $l_{\text{cor}} = L = 3$ m. To obtain realistic results, the wing will be discretized using nine elements for the wing structure and $6 \cdot 10$ elements for the lattice. The response will be obtained from perturbation method at various flow speeds and various bending and torsion stiffness uncertainty levels, i.e.,

$$q_{\text{ben}}(\tau, \theta) = q_{0,\text{ben}}(\tau) + \sum_{n=1}^{N} q_{1,\text{ben}}(\tau)\xi_n(\theta) \tag{25a}$$

$$q_{\text{tor}}(\tau, \theta) = q_{0,\text{tor}}(\tau) + \sum_{n=1}^{N} q_{1,\text{tor}}(\tau)\xi_n(\theta) \tag{25b}$$

where $q_{0,\text{ben}}$ and $q_{0,\text{tor}}$ are obtained from the Eq. (24a), $q_{1,\text{ben}}$ and $q_{1,\text{tor}}$ from the Eq. (24b). The analysis is carried out for $N = 2$, because for $N > 2$ the results converge as shown in Fig. 4. The temporal component of the response variance along the ensemble is given by

$$s^2_{\text{ben}}(t, \theta) = \{q_{\text{ben}}(t, \theta) - E[q_{\text{ben}}(t, \theta)]\}^2 \tag{26a}$$

$$s^2_{\text{tor}}(t, \theta) = \{q_{\text{tor}}(t, \theta) - E[q_{\text{tor}}(t, \theta)]\}^2 \tag{26b}$$

The wing bending and torsion time history records are numerically estimated using Eqs. (25) together with the corresponding variances [as computed from Eqs. (26)] for airflow speed 120 m/s and angle of attack $\alpha = 5$ deg, in the absence of uncertainty. The solutions are obtained for initial conditions $q_{\text{ben}}(0) = -0.05$, $\dot{q}_{\text{ben}}(0) = 0.0$, $q_{\text{tor}}(0) = 0.01$, and $\dot{q}_{\text{tor}}(0) = 0.0$. It is found that the wing is stable under this airflow speed. In the presence of a small level of bending stiffness uncertainty up to $\sigma_{EI_x}/\overline{EI}_x = 0.09$ and zero torsion uncertainty $\sigma_{GJ}/\overline{GJ} = 0.0$, and under the same airflow speed, the wing remains stable and both time history records and their variances decay with time. When the bending stiffness uncertainty reaches the critical value $\sigma_{EI_x}/\overline{EI}_x = 0.1$, the wing experiences instability, loses its zero equilibrium state, and reaches the flutter boundary in the form of LCOs due to aerodynamic nonlinearity. Above that level of bending stiffness uncertainty, the wing oscillations grow without limit. As the airflow speed increases, the flutter boundary takes place for lower values of bending stiffness uncertainty defined by the bound $\sigma_{EI_x}/\overline{EI}_x < 0.1$. An extensive number of numerical solutions have been carried out for the purpose of establishing the flutter boundary on airflow speed V_∞ vs the variance of bending stiffness uncertainty $\sigma_{EI_x}/\overline{EI}_x$. Figure 5a shows the stability bifurcation diagram $V_\infty - \sigma_{EI_x}/\overline{EI}_x$, where the region occupied by small empty circles designates stable wing response, and the region covered by small empty triangles belongs to an unstable wing. The line separating the two regions signals the occurrence of flutter, designated by empty squares.

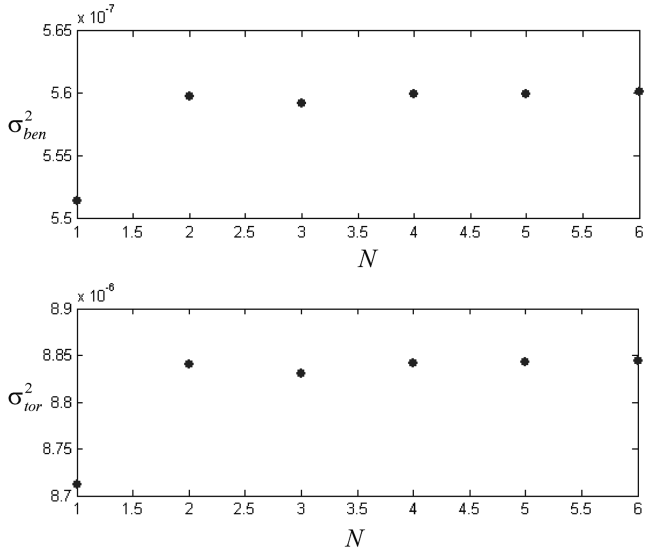

Fig. 4 Dependence of wing response variances on the number of terms N in the Karhunen–Loeve expansion showing the convergence is achieved for $N \geq 2$.

In the absence of bending stiffness uncertainty, and over a small range of torsion stiffness uncertainty, the wing remains stable until $\sigma_{GJ}/\overline{GJ} = 0.035$, at which the wing experiences LCOs for airflow speed 120 m/s; above that level, the wing is unstable. Figure 5b shows the stability bifurcation diagram $V_\infty - \sigma_{GJ}/\overline{GJ}$. It is seen that the stable region in the presence of torsion stiffness uncertainty is smaller than the stable region in the presence of bending stiffness uncertainty. This demonstrates the significant influence of torsion stiffness uncertainty on the stability of the wing.

Figure 6 shows the influence of both bending and torsion uncertainties on the stability of the wing. Figure 6 reveals the stability boundaries for the bending-torsion combination uncertainties $(\sigma_{EI_x}/\overline{EI}_x - \sigma_{GJ}/\overline{GJ})$ at different flow speeds.

VII. Monte Carlo Simulation

To define the limitation of the perturbation method, the Monte Carlo simulation will be performed. First consider the

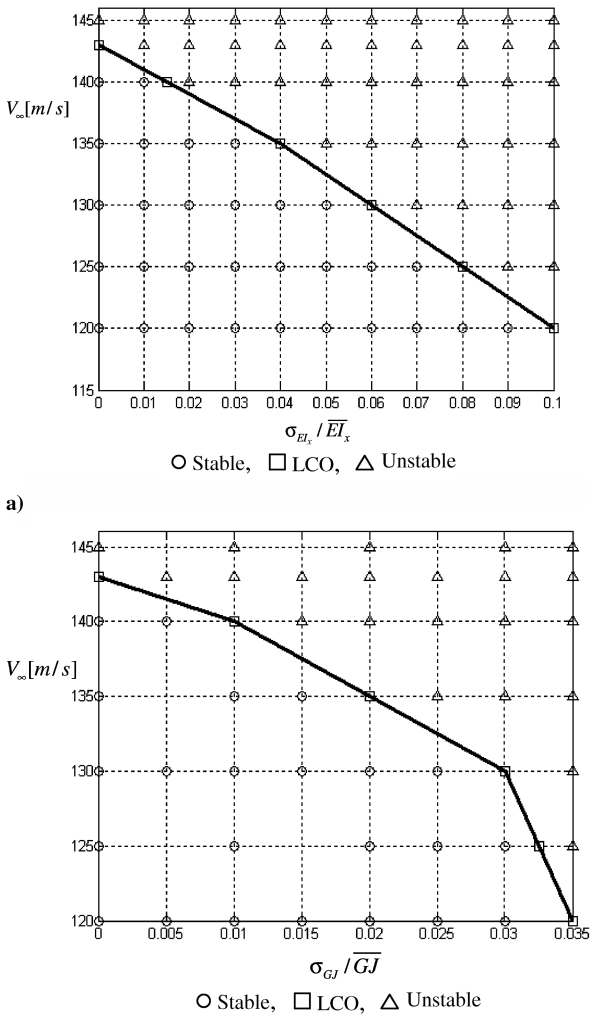

Fig. 5 Stability bifurcation diagram: a) V_∞ vs $\sigma_{EI_x}/\overline{EI}_x$, b) V_∞ vs $\sigma_{GJ}/\overline{GJ}$.

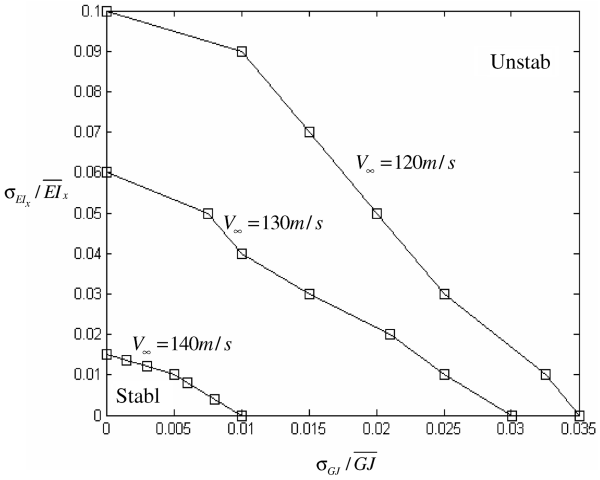

Fig. 6 Stability boundaries $\sigma_{EI_x}/\overline{EI}_x$ vs $\sigma_{GJ}/\overline{GJ}$ at different flow speeds.

deterministic equations of motion for one element as given by Eq. (5). Uncertainties will be introduced in bending stiffness, which is described by Eq. (6a). Assembling the elemental matrices given in Eq. (5), and introducing the aerodynamic loads given by expression (20), gives the system equations of motion:

$$\mathbf{M}\ddot{\mathbf{U}} + \mathbf{K}\mathbf{U} = \mathbf{G}_{SA}\mathbf{F}_A \tag{27}$$

Using the coordinate transformation given by Eq. (23), Eq. (27) takes the form

$$\ddot{\mathbf{q}} + [\mathbf{\Psi}^T\mathbf{K}_0\mathbf{\Psi}]\mathbf{q} = [\mathbf{M}^{-1}\mathbf{\Psi}^{\mathbf{T}}\mathbf{G}_{SA}]\mathbf{F}_A \tag{28}$$

Equation (28) will be integrated numerically once, based on the assumption that the response is ergodic. The Monte Carlo simulation confirms the perturbation results in predicting the LCOs for low values of bending stiffness variance. Figure 7a shows a comparison of perturbation (shown by solid curves) and Monte Carlo simulation (shown by dashed curves) results for bending and torsion variances for flow speed 120 m/s, and stiffness uncertainty parameters $\sigma_{EI_x}/\overline{EI}_x = 0.1$, $\sigma_{GJ}/\overline{GJ} = 0.0$. Figure 7b shows another set for an airflow speed of 140 m/s, bending uncertainty level $\sigma_{EI}/\overline{EI}_x =$ 0.015, and zero torsion uncertainty. Figure 7b reveals good agreement between perturbation and Monte Carlo simulation results.

The bifurcation diagram shown in Fig. 8, obtained from Monte Carlo simulation, is identical with the one shown in Fig. 5 estimated by perturbation method. This demonstrates that the perturbation method is very accurate in the prediction of the LCOs and the establishment of stability boundaries in the presence of bending uncertainties and absence of torsion uncertainties. The dependence of bending and torsion variances on bending uncertainties is shown in Fig. 9 for different values of airflow speed.

Figures 10a and 10b show the Monte Carlo simulation time history response variances for two values of airflow speed, 120 m/s and 140 m/s, and two different levels of torsion stiffness uncertainty, $\sigma_{GJ}/\overline{GJ} = 0.05$ and 0.01, respectively. The comparison shown in Fig. 10a reveals a poor approximation of the perturbation method as compared with Monte Carlo simulation for flow speed 120 m/s and $\sigma_{EI_x}/\overline{EI}_x = 0$, $\sigma_{GJ}/\overline{GJ} = 0.05$.

Note that the Monte Carlo simulation yields LCOs, whereas the perturbation method gives unstable response. Better correlation between the two methods is obtained at higher speeds but lower uncertainty levels, as demonstrated in Fig. 10b for flow speed 140 m/s, $\sigma_{EI_x}/\overline{EI}_x = 0$, $\sigma_{GJ}/\overline{GJ} = 0.01$.

The stability bifurcation diagram $V_\infty - \sigma_{GJ}/\overline{GJ}$ obtained from Monte Carlo simulation is shown in Fig. 11. Comparing the bifurcation diagrams from Figs. 5b and 11, one observes a good correlation in the prediction of LCOs up to flow speed 130 m/s and $\sigma_{GJ}/\overline{GJ} = 0.03$. As the flow speed decreases and torsion stiffness

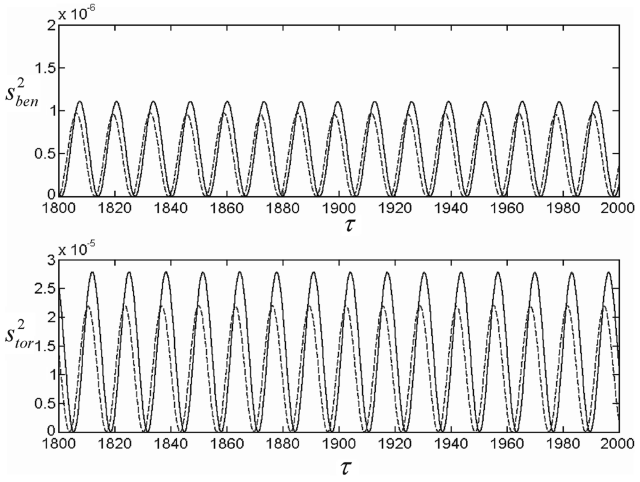

a)

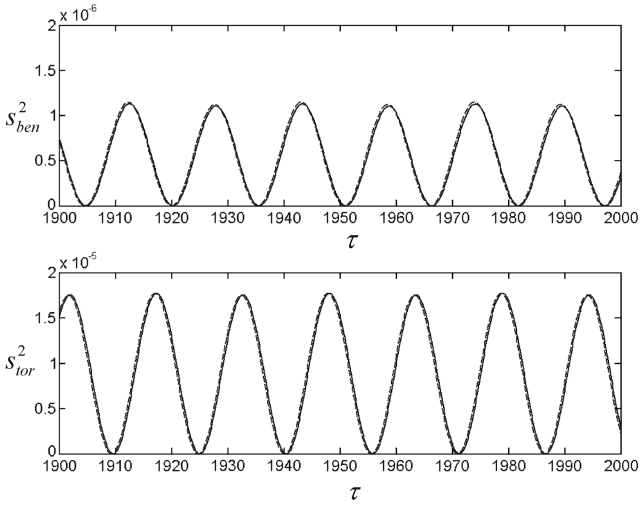

b)

Fig. 7 Time history records of bending and torsion response variance as estimated from perturbation method (solid line) and Monte Carlo simulation (dashed line), for $\alpha_a = 5$ deg, $\sigma_{GJ}/\overline{GJ} = 0$, $q_{\text{ben}}(0) = -0.05$, $\dot{q}_{\text{ben}}(0) = 0$, $q_{\text{tor}}(0) = 0.01$, $\dot{q}_{\text{tor}}(0) = 0$: a) $V_\infty = 120$ m/s, $\sigma_{EI_x}/\overline{EI}_x =$ 0.1; b) $V_\infty = 140$ m/s, $\sigma_{EI_x}/\overline{EI}_x = 0.015$.

uncertainty level increases, the perturbation method loses the ability to predict the LCOs. For example, at flow speed 120 m/s, the flutter onset is obtained from the Monte Carlo simulation at $\sigma_{GJ}/\overline{GJ} =$ 0.05, whereas from the perturbation method at $\sigma_{GJ}/\overline{GJ} = 0.035$.

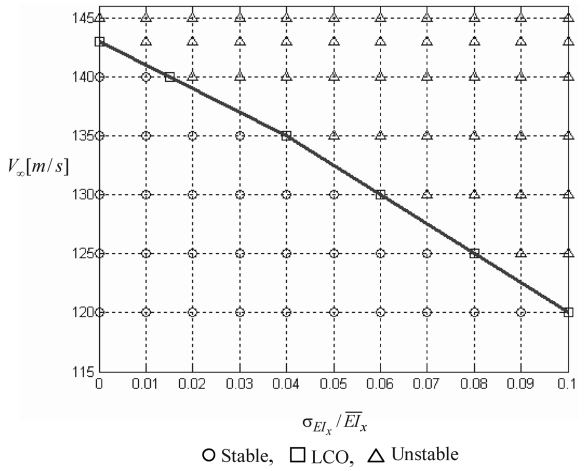

Fig. 8 Stability bifurcation diagram V_∞ vs $\sigma_{EI_x}/\overline{EI}_x$ for Monte Carlo simulation.

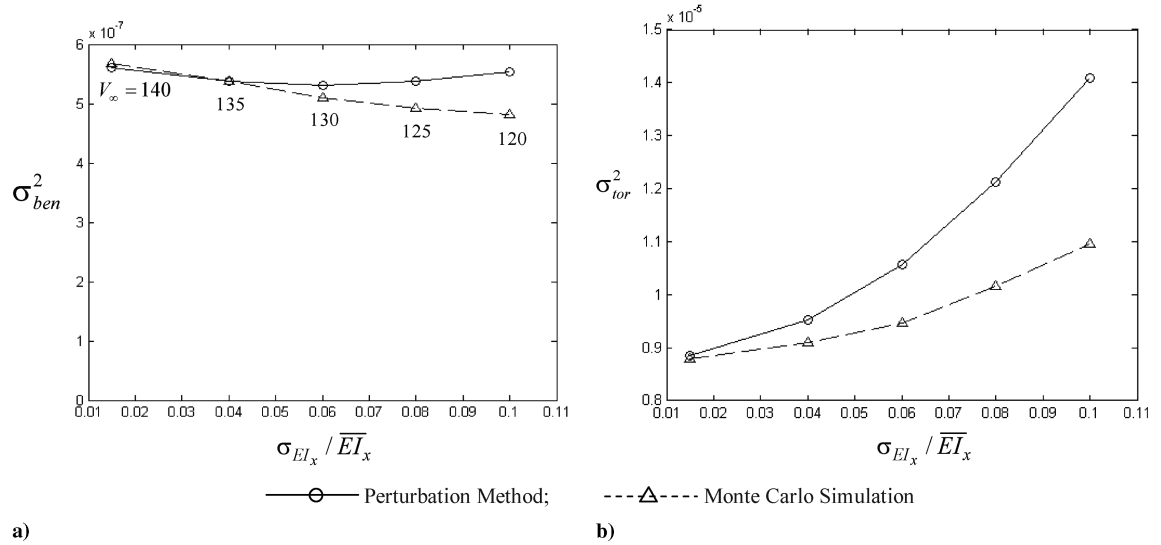

Fig. 9 Comparison of perturbation and Monte Carlo simulation response variances: a) bending, and b) torsion.

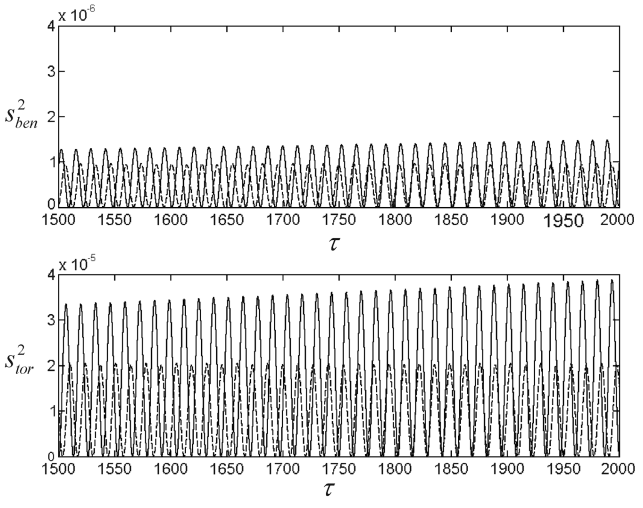

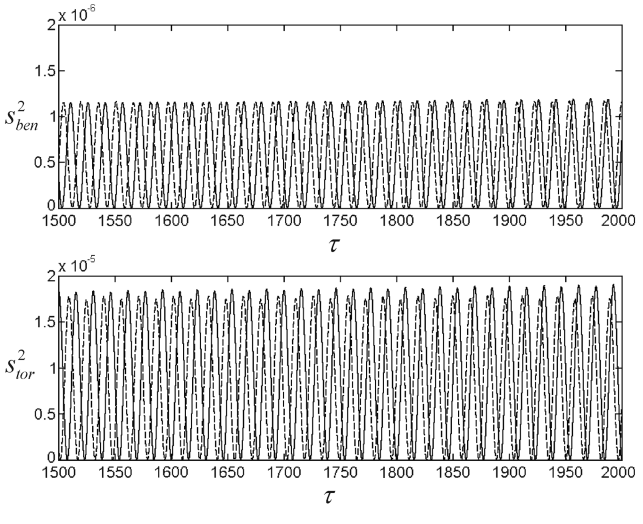

Fig. 10 Time history records of bending and torsion response variances as estimated from perturbation method (solid line) and Monte Carlo simulation (dashed line), for $\alpha_a = 5$ deg, $\sigma_{EI_x}/\overline{EI}_x = 0$, $q_{\text{ben}}(0) = -0.05$, $\dot{q}_{\text{ben}}(0) = 0$, $q_{\text{tor}}(0) = 0.01$, $\dot{q}_{\text{tor}}(0) = 0$: a) $V_\infty = 120$ m/s, $\sigma_{GJ}/\overline{GJ} = 0.05$; b) $V_\infty = 140$ m/s, $\sigma_{GJ}/\overline{GJ} = 0.01$.

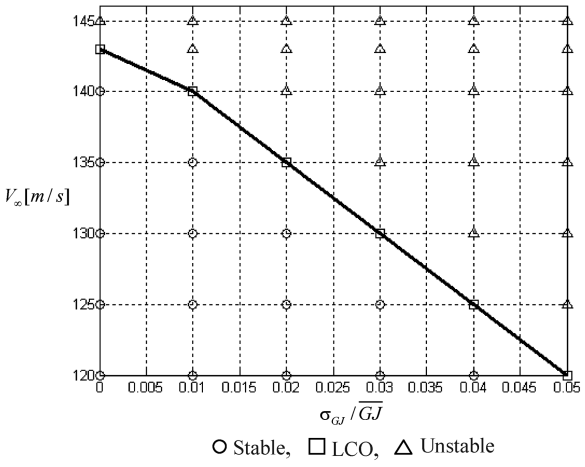

Fig. 11 Stability bifurcation diagram V_∞ vs $\sigma_{GJ}/\overline{GJ}$ for Monte Carlo simulation.

Figure 12 shows the dependence of bending and torsion variances on the torsion stiffness uncertainty level for different values of airflow speed indicated on each curve. Both diagrams reveal the validity of the perturbation method for a low level of stiffness uncertainty.

VIII. Conclusions

The influence of uncertainties of bending and torsion stiffness parameters on the flutter behavior of an aeroelastic wing is examined. The uncertainties are modeled using a modified first-order stochastic perturbation method together with a truncated Karhunen–Loeve expansion instead of Taylor series. However, the Taylor series is used for displacement vector expansion. The results of the perturbation approach are compared with those predicted by Monte Carlo simulation, and the comparison revealed good correlation for low values of stiffness uncertainty levels. As the uncertainty level increases, the perturbation method loses accuracy. For the prediction of LCO, the perturbation method is very accurate for all levels of bending stiffness uncertainty examined, but the method loses its accuracy at upper levels of torsion stiffness uncertainty. The stability boundary in the flow speed vs stiffness uncertainty reveals the appearance of LCOs below the flutter speed. Further increase of uncertainty level produces instability. The uncertainties in torsion stiffness induce a greater disturbance in the

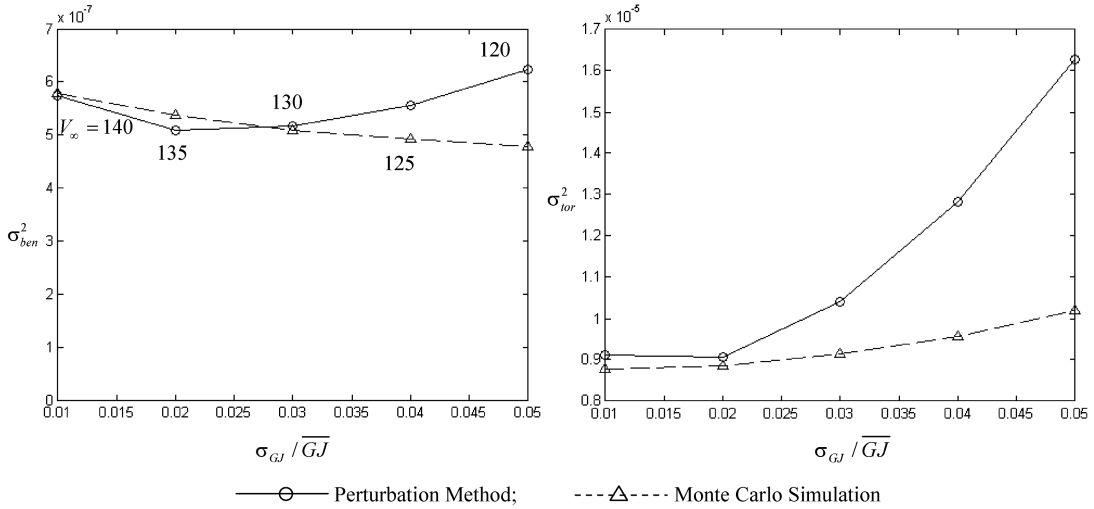

Fig. 12 Perturbation method convergence.

system. A smaller level of torsion stiffness uncertainty induces instability in the system.

Appendix: Detailed Structures of Y_{ij} of Eq. (17)

$$\mathbf{Y}_{11} = \begin{bmatrix} Y_3 & 0 & 0 \\ 0 & Y_1 & 0 \\ 0 & 0 & Y_3 \end{bmatrix}, \qquad \mathbf{Y}_{12} = \begin{bmatrix} 0 & 0 & -Y_5 \\ 0 & 0 & 0 \\ Y_5 & 0 & 0 \end{bmatrix}$$

$$\mathbf{Y}_{13} = \begin{bmatrix} Y_4 & 0 & 0 \\ 0 & Y_2 & 0 \\ 0 & 0 & Y_4 \end{bmatrix}, \qquad \mathbf{Y}_{14} = \begin{bmatrix} 0 & 0 & -Y_6 \\ 0 & 0 & 0 \\ Y_6 & 0 & 0 \end{bmatrix}$$

$$\mathbf{Y}_{21} = \begin{bmatrix} 0 & 0 & -Y_3' \\ 0 & 0 & 0 \\ Y_3' & 0 & 0 \end{bmatrix}, \qquad \mathbf{Y}_{22} = \begin{bmatrix} Y_5' & 0 & 0 \\ 0 & Y_1 & 0 \\ 0 & 0 & Y_5' \end{bmatrix}$$

$$\mathbf{Y}_{23} = \begin{bmatrix} 0 & 0 & -Y_4' \\ 0 & 0 & 0 \\ Y_4' & 0 & 0 \end{bmatrix}, \qquad \mathbf{Y}_{24} = \begin{bmatrix} Y_6' & 0 & 0 \\ 0 & Y_2 & 0 \\ 0 & 0 & Y_6' \end{bmatrix}$$

where a prime denotes a derivative with respect to y and Y_i are the finite element shape functions given by

$$Y_1 = \frac{y_{i+1} - y}{y_{i+1} - y_i}, \qquad Y_2 = \frac{y - y_i}{y_{i+1} - y_i}$$

$$Y_3 = 1 - 3\left(\frac{y - y_i}{y_{i+1} - y_i}\right)^2 + 2\left(\frac{y - y_i}{y_{i+1} - y_i}\right)^3$$

$$Y_4 = 3\left(\frac{y - y_i}{y_{i+1} - y_i}\right)^2 - 2\left(\frac{y - y_i}{y_{i+1} - y_i}\right)^3$$

$$Y_5 = (y - y_i) - \frac{2}{y_{i+1} - y_i}(y - y_i)^2 + \frac{1}{(y_{i+1} - y_i)^2}(y - y_i)^3$$

$$Y_6 = -\frac{1}{y_{i+1} - y_i}(y - y_i)^2 + \frac{1}{(y_{i+1} - y_i)^2}(y - y_i)^3$$

$$y_i \le y \le y_{i+1}$$

Acknowledgment

This research is supported by a grant from the U.S. Air Force Office of Scientific Research under grant number FA9550-04-1-0042. Victor Giurgiutiu is the Program Director.

References

[1] Ibrahim, R. A., "Structural Dynamics with Parameter Uncertainties," *Applied Mechanics Reviews*, Vol. 40, No. 3, 1987, pp. 309–328.

[2] Manohar, C. S., and Ibrahim, R. A., "Progress in Structural Dynamics with Stochastic Parameter Variations: 1987–1998," *Applied Mechanics Reviews*, Vol. 52, No. 5, 1999, pp. 177–196.

[3] Pettit, C. L., "Uncertainty Quantification in Aeroelasticity: Recent Results and Research Challenges," *Journal of Aircraft*, Vol. 41, No. 5, 2004, pp. 1217–1229.

[4] Bae, H. R., Grandhi, R. V., and Canfield, R. A., "Approximation Approach for Uncertainty Quantification Using Evidence Theory," *Reliability Engineering and System Safety*, Vol. 86, No. 3, Dec. 2004, pp. 215–235.

[5] Beran, P. S., Pettit, C. L., and Millman, D. R., "Uncertainty Quantification of Limit-Cycle Oscillations," *Journal of Computational Physics*, Vol. 217, No. 1, 2006, pp. 217–247. doi:10.1016/j.jcp.2006.03.038

[6] Ghanem, G. G., and Spanos, P. D., *Stochastic Finite Elements: A Spectral Approach*, Springer–Verlag, New York, 1991.

[7] Kleiber, M., Tran, D. H., and Hien, T. D., *Stochastic Finite Element Method*, Wiley, New York, 1992.

[8] Cambou, B., "Application of First-Order Uncertainty Analysis in the Finite Element Method in Linear Elasticity," *Proceedings of the 2nd International Conference on Application of Statistics and Probability in Soil and Structural Engineering*, Inst. of Electrical and Electronics Engineers, New York, 1975, pp. 67–87.

[9] Nakagiri, S., and Hisada, T., "Stochastic Finite Element Method Applied to Structural Analysis with Uncertain Parameters," *Proceedings of the International Conference on Finite Element Method*, Univ. of Melbourne, Parkville, Victorial, Auston, Australia, 1982, pp. 206–211.

[10] Shinozuka, M., and Yamazaki, F., "Stochastic Finite Element Analysis: An Introduction," *Stochastic Structural Dynamics: Progress in Theory and Applications*, edited by S. T. Ariaratnam, G. I. Schueller, and I. Elishakoff, Elsevier Applied Science, London, Chap. 14, 1988, pp. 241–291.

[11] Liu, W. K., Belytschko, T., and Mani, A., "Probabilistic Finite Elements for Nonlinear Structural Dynamics," *Computer Methods in Applied Mechanics and Engineering*, Vol. 56, No. 1, 1986, pp. 61–81. doi:10.1016/0045-7825(86)90136-2

[12] Yamazaki, F., Shinozuka, M., and Dasgupta, G., "Neumann Expansion for Stochastic Finite Element Analysis," *Journal of Engineering Mechanics*, Vol. 114, No. 8, 1988, pp. 1335–1354.

[13] Nieuwenhof, B. V. D., and Coyette, J.-P., "Perturbation Stochastic Finite Element Method for the Time-Harmonic Analysis of Structures with Random Mechanical Properties," *Proceedings of the 5th World Congress on Computational Mechanics*, European Commission, Luxemburg, Germany, 2002.

[14] Muscolino, G., Ricciardi, G., and Impollonia, N., "Improved Dynamic Analysis of Structures with Mechanical Uncertainties Under Deterministic Input," *Probabilistic Engineering Mechanics*, Vol. 15, No. 2, 2000, pp. 199–212. doi:10.1016/S0266-8920(99)00021-1

[15] Cacciola, P., and Muscolino, G., "Dynamic Response of a Rectangular Beam with a Known Non-Propagating Crack of Certain and Uncertain Depth," *Computers and Structures*, Vol. 80, Nos. 27–30, 2002, pp. 2387–2396. doi:10.1016/S0045-7949(02)00255-9

[16] Jensen, H. A., "Dynamic Response of Structures with Uncertain

Parameters," Ph.D. Dissertation, California Inst. of Technology, Pasadena, CA, 1990.
[17] Lei, Z., and Qiu, C., "Neumann Dynamic Stochastic Finite Element Method of Vibration for Structures with Stochastic Parameters to Random Excitation," *Computers and Structures*, Vol. 77, No. 6, 2000, pp. 651–657. doi:10.1016/S0045-7949(00)00019-5
[18] Liaw, D. G., and Yang, H. T. Y., "Reliability of Uncertain Laminated Shells Due to Buckling and Supersonic Flutter," *AIAA Journal*, Vol. 29, No. 10, 1991, pp. 1698–1708.
[19] Liaw, D. G., and Yang, H. T. Y., "Reliability of Initially Compressed Uncertain Laminated Plates in Supersonic Flow," *AIAA Journal*, Vol. 29, No. 6, 1991, pp. 952–960.
[20] Kuttenkeuler, J., and Ringertz, U., "Aeroelastic Tailoring Considering Uncertainties in Material Properties," *Structural Optimization*, Vol. 15, Nos. 3–4, 1998, pp. 157–162. doi:10.1007/BF01203526
[21] Lindsley, N. J., Beran, P. S., and Pettit, C. L., "Effects of Uncertainty on the Aerothermoelastic Flutter Boundary of a Nonlinear Plate," AIAA Paper 2002-5136, 2002.
[22] Lindsley, N. J., Beran, P. S., and Pettit, C. L., "Effects of Uncertainty on Nonlinear Plate Aeroelastic Response," AIAA Paper 2002-1271, 2002.
[23] Poirion, F., "Impact of Random Uncertainty on Aircraft Aeroelastic Stability," *Proceedings of the 3rd International Conference on Stochastic Structural Dynamics*, CRC Press, Boca Raton, FL, 1995.
[24] Poirion, F., "On Some Stochastic Methods Applied to Aeroservoelasticity," *Aerospace Science and Technology*, Vol. 4, No. 3, 2000, pp. 201–214. doi:10.1016/S1270-9638(00)00118-8
[25] Pettit, C. L., and Beran, P. S., "Effects of Parametric Uncertainty on Airfoil Limit-Cycle Oscillation," *Journal of Aircraft*, Vol. 40, No. 5, 2003, pp. 1004–1006.
[26] Pettit, C. L., and Beran, P. S., "Polynomial Chaos Expansion Applied to Airfoil Limit-Cycle Oscillations," *Collection of Technical Papers: AIAA/ASME/ASCE/AHS/ASC Structures, Structural Dynamics and Materials Conference*, 1975–1985, 2004.
[27] Ueda, T., "Aeroelastic Analysis Considering Structural Uncertainty," *Aviation*, Vol. 9, No. 1, 2005, pp. 3–7.
[28] Attar, P. J., and Dowell, E. H., "Stochastic Analysis of the Limit-Cycle Behavior of a Nonlinear Aeroelastic Model Using the Response Surface Method," *Proceedings of the 46th AIAA/ASME/ASCE/AHS/ASC Structures, Structural Dynamics and Materials Conference*, AIAA Paper No. 2005-1986, 2005, pp. 2318–2338.
[29] Ostenfeld-Rosenthal, P., Madsen, H. O., and Larsen, A., "Probabilistic Flutter Criteria for Long Span Bridges," *Journal of Wind Engineering and Industrial Aerodynamics*, Vol. 42, Nos. 1–3, 1992, pp. 1265–1276. doi:10.1016/0167-6105(92)90133-U
[30] Ge, Y. J., Xiang, H. F., and Tanaka, H., "Application of the Reliability Analysis Model to Bridge Flutter Under Extreme Winds," *Journal of Wind Engineering and Industrial Aerodynamics*, Vol. 86, No. 2, 2000, pp. 155–167. doi:10.1016/S0167-6105(00)00008-8
[31] Jakobsen, J. B., and Tanaka, H., "Modeling Uncertainties in Prediction of Aeroelastic Bridge Behavior," *Journal of Wind Engineering and Industrial Aerodynamics*, Vol. 91, Nos. 12–15, 2003, pp. 1485–1498. doi:10.1016/j.jweia.2003.09.006
[32] Kareem, A., "Aerodynamic Response of Structures with Parameter Uncertainties," *Structural Safety*, Vol. 5, No. 3, 1988, pp. 205–225. doi:10.1016/0167-4730(88)90010-0
[33] Potter, S., and Lind, R., "Developing Uncertainty Models for Robust Flutter Analysis Using Ground Vibration Test Data," NASA TM-2001-210392, 2001.
[34] Lind, R., and Brenner, M., "Flutterometer: An On-Line Tool to Predict Robust Flutter Margins," *Journal of Aircraft*, Vol. 37, No. 6, 2000, pp. 1105–1112.
[35] Brenner, M. J., "Aeroservoelastic Uncertainty Model Identification from Flight Data," *Journal of Guidance, Control, and Dynamics*, Vol. 25, No. 4, 2002, pp. 748–754.
[36] Prazenica, R. J., Lind, R., and Kurdila, A. J., "Uncertainty Estimation from Volterra Kernels for Robust Flutter Analysis," *Journal of Guidance, Control, and Dynamics*, Vol. 26, No. 2, 2003, pp. 331–339.
[37] Preidikman, S., and Mook, D., "Time-Domain Simulations of Linear and Nonlinear Aeroelastic Behavior," *Journal of Vibration and Control*, Vol. 6, No. 8, 2000, pp. 1135–1175. doi:10.1177/107754630000600802
[38] Preidikman, S., "Numerical Simulations of Interactions Among Aerodynamics, Structural Dynamics, and Control Systems," Ph.D. Dissertation, Virginia Polytechnic Inst. and State Univ., Blacksburg, VA, 1998.
[39] Chandrupatla, T. R., and Belegundu, A. D., *Introduction to Finite Elements in Engineering*, Prentice–Hall, Upper Saddle River, NJ, 2002.
[40] Curtis, H. D., *Fundamentals of Aircraft Structural Analysis*, McGraw–Hill, New York, 1997.
[41] Huang, S. P., Quek, S. T., and Phoon, K. K., "Convergence Study of the Truncated Karhunen–Loeve Expansion for Simulation of Stochastic Processes," *International Journal for Numerical Methods in Engineering*, Vol. 52, 2001, pp. 1029–1043. doi:10.1002/nme.255
[42] Loeve, M., *Probability Theory*, Springer–Verlag, Berlin, 1977.
[43] Hall, B. D., "Numerical Simulations of the Aeroelastic Response of an Actively Controlled Flexible Wing," M.S. Thesis in Engineering Mechanics, Virginia Polytechnic Inst. and State Univ., Blacksburg, VA, 1999.

E. Livne
Associate Editor